Journal of Power Sources 196 (2011) 4193–4199

Contents lists available at ScienceDirect

Journal of Power Sources

journal homepage: www.elsevier.com/locate/jpowsour

Homolytic cleavage C–C bond in the electrooxidation of ethanol and bioethanol

J. Barroso[a,*], A.R. Pierna[a,1], T.C. Blanco[a], E. Morallón[b], F. Huerta[c]

[a] Dept. Ingeniería Química y del Medio Ambiente, Universidad del País Vasco, Plaza de Europa 1, CP 20018, San Sebastián, Spain
[b] Dept. Química Física, Universidad de Alicante, Apartado 99, E-03080 Alicante, Spain
[c] Dept. Ingeniería Textil y Papelera, Universidad Politécnica de Valencia, Plaza Ferrándiz y Carbonell 1, E-03801 Alcoy, Spain

ARTICLE INFO

Article history:
Received 30 July 2010
Received in revised form
16 September 2010
Accepted 29 September 2010
Available online 7 October 2010

Keywords:
Bi-catalytic catalysts
Ethanol
Bioethanol
Electrooxidation
Acetic acid
CO_2

ABSTRACT

Nowadays, the studies are focused on the search of better electrocatalysts that promote the complete oxidation of ethanol/bioethanol to CO_2. To that end, amorphous bi-catalytic catalysts of composition $Ni_{59}Nb_{40}Pt_{1-x}Y_x$ (Y = Cu, Ru, x = 0.4% at.) have been developed, obtained by mechanical alloying, resulting in higher current densities and an improvement in tolerance to adsorbed CO vs. $Ni_{59}Nb_{40}Pt_1$ catalyst. By using voltammetric techniques, the appearance of three oxidation peaks can be observed. The first peak could be associated with the electrooxidative process of ethanol/bioethanol to acetaldehyde, the second peak could be the oxidation of acetaldehyde to acetic acid, and the last peak might be the final oxidation to CO_2. Chrono-amperometric experiments show qualitative poisoning of catalytic surfaces. However, the in situ Fourier Transformed Infrared Spectroscopy, FTIR, is used for the quasi-quantitative determination with which can be observed the appearance and evolution of different vibrational bands of carbonyl and carboxylic groups of different species, as it moves towards anodic potential in the electrooxidative process.

1. Introduction

Nowadays, there is a wide interest in the development of fuel cells of direct ethanol (DEFCs), and the employment of ethanol and/or bioethanol as renewable and sustainable fuel with the environment, is in its heyday. The completed electrooxidation of ethanol/bioethanol to CO_2 [1,2] involves the transference of 12 electrons in the anodic reaction (1), as follows:

$$CH_3CH_2OH + 3H_2O \rightarrow 2CO_2 + 12H^+ + 12e^- \quad (1)$$

However, the homolytic cleavage of C–C bond is the determining stage of electrooxidative process, limiting the electronic transfer to 4 electrons, as follow in reaction (2):

$$CH_3CH_2OH + H_2O \rightarrow CH_3COOH + 4H^+ + 4e^- \quad (2)$$

Considering working conditions, for a DEFC at 0.5 V at 50 mA cm^{-2} with complete oxidation to CO_2, the energy efficiency (3) would be:

$$\varepsilon_{cell}^{C_2H_5OH/O_2} = \frac{\eta_{exp} FE(|j|)}{-\Delta H^0} = \varepsilon_{eq}^{rev} \times \varepsilon_E \times \varepsilon_F = \frac{W_{el}}{(-\Delta H^0)} \times \frac{E_{work}}{E_{eq}^0} \times \frac{\eta_{exp}}{\eta_{th}} = 0.424 \quad (3)$$

If the electrooxidative process stops at the acetic acid, which involves 4 electrons instead of 12 electrons, the energy efficiency will be reduced by one third, being only 0.14. Therefore, the real electric efficiency obtained with the DEFCs, are below 50% [3]. The cell voltage $E(j)$ decreases greatly due to three limiting factors: the charge transfer overvoltages at the anode and cathode, the ohmic drop in the electrolyte and interface, and the mass transfer limitations for reactants and products.

To get a higher conversion of chemical energy in electricity, the search of better electrocatalysts is necessary [4]. The nature and structure of these new electrodic materials affect the electrooxidative process, controlling the formation of adsorbed species and final products, and favouring the cleavage of C–C bond. Nowadays, one of the most important research activities is the development of Pt catalysts. Platinum is regarded as the most active material for ethanol/bioethanol electrooxidation, especially in acid media, which is the only active and stable noble metal. However, its global shortage makes it very expensive. In addition, the platinum itself is known for the fast poisoning of its surface, especially for CO. Previous electrochemical works have been carried out on metal–metal glasses, but few studies have focused on $Ni_{60}Nb_{40}$ based amorphous alloys. These metals are alloyed with platinum, which are used as anodic materials for electrochemical treatments of different toxic compounds and for its application in fuel cells [5,6]. The amorphous

* Corresponding author. Tel.: +34 943 017 127, fax: +34 943 017 131.
E-mail addresses: jbarroso003@ikasle.ehu.es, javierbarrosolazaro@yahoo.es (J. Barroso), iapropia@sp.ehu.es (A.R. Pierna).
[1] Tel.: +34 943 017 183.

0378-7753/$ – see front matter © 2010 Elsevier B.V. All rights reserved.
doi:10.1016/j.jpowsour.2010.09.087

state is more active than the crystalline, with a greater density of active surface areas. It also reduces the amount of platinum and, therefore, the overall cost of the catalysts.

The researches have focused on the search and development of metallic amorphous microparticulated alloys of composition $Ni_{59}Nb_{40}Pt_{1-x}Y_x$ (Y = Metal; x = 0.4% at.). The addition of the second metal as co-catalysts, modifies the electronic properties of platinum, which can be explained by the bi-functional mechanisms and electronic densities. First of all, the presence of second metal alloying with Pt [7–9] would dissociate water molecule, forming hydroxylated species to more cathodic potential, which will ease the oxidation reaction (4) of CO to CO_2:

$$\begin{aligned} &M + H_2O \rightarrow M(OH)_{ads} + H^+ + e^- \ (M = Pt, Cu, Ru) \\ &M(CO)_{ads} + M(OH)_{ads} \rightarrow 2M + CO_2 + H^+ + e^- \end{aligned} \quad (4)$$

On the other hand, by electronic effects, it produces a ligand effect, generating a positive shift in the binding energy of 4f or 4d orbital of platinum, generating an increase of vacancies in the 5d orbital, resulting in a minor effect on the electron donor under molecules of CO, decreasing the monolayer adsorbed on the catalyst surface [10,11].

Adsorption and oxidation of ethanol/bioethanol in Pt catalysts has been the object of numerous studies for the last 25 years, but the exact mechanism of the anodic reaction is still not known, because it occurs in several stages. In the present paper, an investigation into catalytic activities and kinetics of ethanol/bioethanol on $Ni_{59}Nb_{40}Pt_{0.6}Cu_{0.4}$ and $Ni_{59}Nb_{40}Pt_{0.6}Ru_{0.4}$ was performed by different electrochemical and in situ (FTIR) techniques.

2. Experimental

2.1. Electrodes and solutions

The amorphous metallic microparticulated alloys of atomic composition $Ni_{59}Nb_{40}Pt_{0.6}Cu_{0.4}$ and $Ni_{59}Nb_{40}Pt_{0.6}Ru_{0.4}$ were achieved by using a planetary mill (Retsch 400 PM) during 40 h. The known amounts of different metals were placed in a stainless steel vial together with balls of the same material in a ratio of 1:4. Subsequently, as soon as the time of alloying was finished, the obtained alloys are sieved to obtain the size of the desired particles. For this, it used a test sieve (CISA Cedacería Industrial). By standard sieves with openings of 50 μm and 20 μm, the sizes of desired particles are achieved for the electrocatalytic study of present work. The prepared electrocatalysts were characterized through the techniques of Differential Scanning Calorimetry (DSC), X-Ray Diffraction (XRD) and Scanning Electron Microscopy (SEM) to verify their amorphous nature. The Energy Dispersive X-Ray Spectroscopy (EDX) was used for the chemical analysis.

$Ni_{59}Nb_{40}Pt_{0.6}Cu_{0.4}$ and $Ni_{59}Nb_{40}Pt_{0.6}Ru_{0.4}$ alloys were suspended in ethanol, ultra-pure water and Nafion 5 WT % for FTIR studies. These solutions were placed on a gold disc and dried using IR light. Later, they were also chemically activated in HF 48% (PA, Panreac). The solutions employed for the in situ FTIR spectroscopy experiments were 0.1 M $HClO_4$ (Merck Suprapur), 0.1 M Ethanol (PA, Panreac) and D_2O (Sigma–Aldrich).

Modified carbon paste electrodes (MCPEs) were made by hand-mixing the microparticulated alloy with glassy carbon powder (Aldrich, 2–12 μm), and paraffin (Uvasol®, Merck), as binder. The alloys were chemically activated in HF 48% (PA, Panreac) and rinsed out successively with doubled-distilled water. All preparations were performed at room temperature. After that, and before any electrochemical experiment, the uniformity of the catalytic behavior was tested by cycling such electrodes several times during a cyclic voltammetry experience in 0.1 M $HClO_4$ as supporting electrolyte, until a repetitive voltammogram was achieved.

2.2. Experimental set up

Electrochemical characterization techniques were cyclic voltammetry and chronoamperometry. The electrochemical setup consists in a flow cell of a single compartment with a three-electrode system. The working electrode had a geometric area of 0.28 cm^2. The used counter electrode was a glassy high area carbon electrode. A commercial Ag/AgCl electrode was used as the reference electrode (207 mV vs. NHE), against which all potential values were referenced. The electrochemical measurements were performed using a multipotentiostat Solartron 1480, driven by a Corrware® Software program.

The in situ FTIR experiments were carried out with a Nicolet Magna 850 spectrometer equipped with nitrogen cooled MCT detector. The system is controlled by a computer driven by ONMIC Software. The spectroelectrochemical cell was provided with a prismatic CaF_2 window bevelled at 60°. The experimental set-up allows the electrochemical characterization of the system prior to the FTIR experiment. The used working electrode and counter electrode was gold. All potentials were measured against a reversible hydrogen electrode (RHE) immersed in the test solutions and are presented in this scale. The interferograms were acquired with the working electrode surface pressed against the window. Unless otherwise stated, p-polarized radiation was used. All the spectra were recorded with a resolution of 8 cm^{-1} and presented in the usual form $\Delta R/R$.

All DSC measures were carried out using a Modulated Differential Scanning Calorimeter DSC 2920 CE (TA instruments) with a standard cell model 2920 MDSC. The instrument is controlled by a computer driven by a TA control instrument software. The obtained thermograms were analyzed by means of the Universal TA Analysis software. XRD was performed using a Philips X'Pert Pro powder diffractometer working with CuKα radiation (λ = 1.54 Å). This equipment allowed registering the diffractograms in the 2 h range from 5° to 120° in 2.3 min, avoiding the significant absorption of the atmospheric water during the measurements. The obtained patterns were normalized in the high q-range where the intensity cannot vary between the different samples owing to the very short structural distances responsible for the scattering in this region. The SEM images were taken at scanning electron microscope JEOL, model JSM-6400, equipped with EDX microanalysis (Oxford Link EXL II) and WDX (2 spec. JEOL) to determine the atomic composition.

3. Results and discussion

3.1. Physical characterization

The main characteristics of these metallic microparticulated alloys consist on single phase systems with high chemical homogeneity, and which are achieved with higher specific surfaces. The better atomic composition of alloys was described by Barranco and Pierna [7–9]. Fig. 1 shows DSC thermograms of $Ni_{59}Nb_{40}Pt_{0.6}Cu_{0.4}$ and $Ni_{59}Nb_{40}Pt_{0.6}Ru_{0.4}$ alloys after 40 h of mechanical alloying. In relation to the amorphous phases, one peak can be clearly observed at 679.40 °C and 663.47 °C for $Ni_{59}Nb_{40}Pt_{0.6}Cu_{0.4}$ and $Ni_{59}Nb_{40}Pt_{0.6}Ru_{0.4}$ alloys respectively. Due to the different thermal stability there may occur shifts between 10 and 20 °C of these peaks, depending on the type of element that is alloying with the $Ni_{60}Nb_{40}$. These peaks are related to exothermic process corresponding to the crystallization of the amorphous phases present in alloys. Ternary Ni_3Nb phase structure can assign to these peaks [8]. At this composition, the different crystallized products are the same as the results of Lee et al. and Koch et al. [12,13].

X-ray diffraction patterns for $Ni_{59}Nb_{40}Pt_{0.6}Cu_{0.4}$ and $Ni_{59}Nb_{40}Pt_{0.6}Ru_{0.4}$ alloys are shown in Fig. 2. Both alloys have a

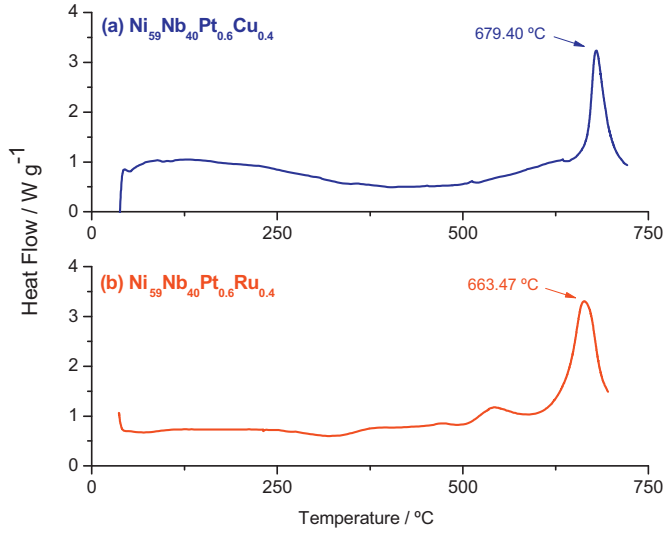

Fig. 1. DSC traces after 40 h milling time, obtained at a constant heating rate of 10 °C min^{-1} in N_2 atmosphere for (a) $Ni_{59}Nb_{40}Pt_{0.6}Cu_{0.4}$ alloy and (b) $Ni_{59}Nb_{40}Pt_{0.6}Ru_{0.4}$ alloy.

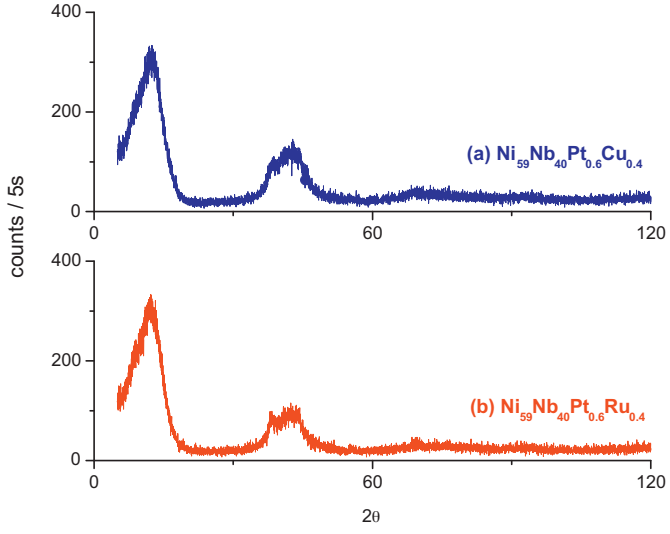

Fig. 2. X-ray diffraction patterns of amorphous (a) $Ni_{59}Nb_{40}Pt_{0.6}Cu_{0.4}$ alloy and (b) $Ni_{59}Nb_{40}Pt_{0.6}Ru_{0.4}$ alloy after 40 h of mechanical alloying.

high Ni–Nb composition which is of great importance to obtain the amorphous nature, due to the presence of an eutectic point in the $Ni_{60}Nb_{40}$ composition in the phase diagram. In both cases, XRD patterns show two characteristic peaks, the first one is related to support material, and the second one shows the amorphousness of the alloys. The presence of a wide halo indicates the absence of crystalline structure. Barranco and Pierna [8] shows the loss of crystallinity of different metals, no appearing crystallization peaks.

Table 1
Average values obtained by EDX microanalysis for the elements of (a) $Ni_{59}Nb_{40}Pt_{0.6}Cu_{0.4}$ and (b) $Ni_{59}Nb_{40}Pt_{0.6}Ru_{0.4}$ alloys.

	Composition (% atomic)				
	Ni	Nb	Pt	Cu	Ru
(a) $Ni_{59}Nb_{40}Pt_{0.6}Cu_{0.4}$	58.92	40.12	0.58	0.38	0.00
(b) $Ni_{59}Nb_{40}Pt_{0.6}Ru_{0.4}$	59.20	39.83	0.62	0.00	0.35

Fig. 3 shows SEM images. The morphology of both alloys presents irregular particles, mainly spheroids, of different sizes, ranging between 20 and 50 μm, being slightly smaller than 20 μm. A rough consistency with little pores can be observed. In Table 1, it can observe the average values of composition in % atomic for different particles of both alloys, not having variations in the theoretical atomic composition. Therefore, both alloys show homogeneity in their atomic composition.

3.2. Electrochemical characterization

3.2.1. Activation time

Metallic alloys in "as-quenched" state are not active, therefore they must be previously chemically activated [14,15] using 48% HF, with the aim of pickling of the nickel and niobium oxides (Nb_2O_5) formed during the manufacturing process. Once activated and rinsed out with distilled water, the electrodes are kept in distilled water and deaerated with nitrogen, to prevent the formation of oxide layers.

One parameter that must be taken into account for the correct characterization of these electrodes is the previous determination of the optimum times of chemical activation. The degree of optimal activation was determined according to the available catalytic area after activation. This area was measured by cyclic voltammetry tests in 0.1 M $HClO_4$, by integrating the flow of adsorption/desorption of hydrogen, assuming a charge of 210 μC for 1 cm^{-2} of platinum area [16]. All the current density values were normalized by this catalytic area. All in all, it was determined that the optimal time of activation for $Ni_{59}Nb_{40}Pt_{0.6}Cu_{0.4}$ alloy was 12 s and for $Ni_{59}Nb_{40}Pt_{0.6}Ru_{0.4}$ alloy was 5 s. The lower the activation time is, the lower availability of catalytic surfaces there are. On the other hand, if the activation time was high, the lost of catalytic material might occur. Furthermore, the formation of new compounds might also block the catalytic surface.

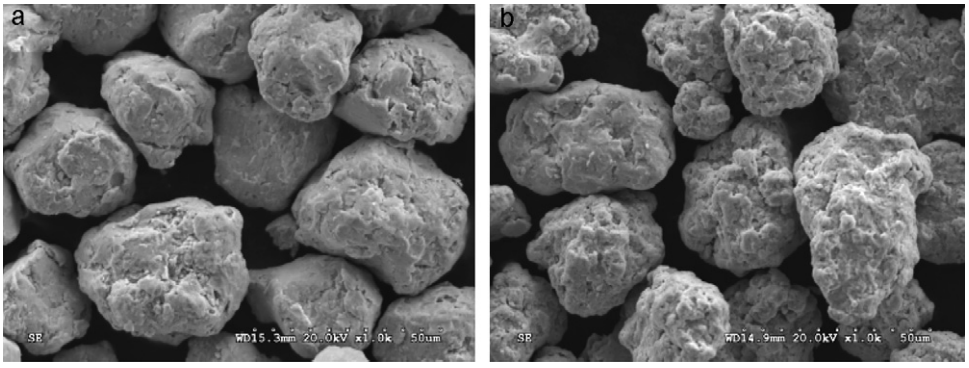

Fig. 3. SEM of (a) $Ni_{59}Nb_{40}Pt_{0.6}Cu_{0.4}$ alloy and (b) $Ni_{59}Nb_{40}Pt_{0.6}Ru_{0.4}$ alloy.

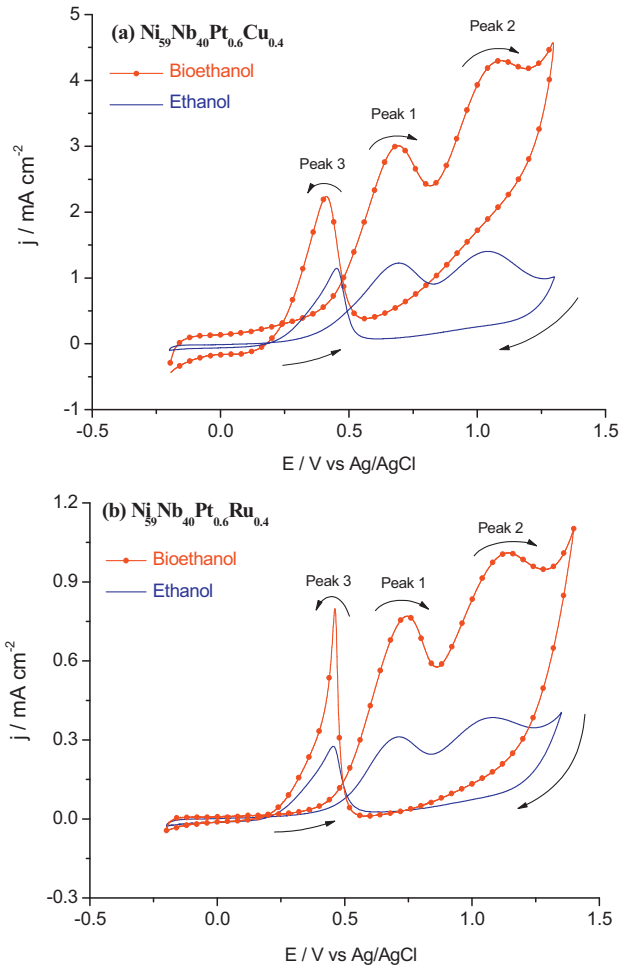

Fig. 4. Voltammograms showing the oxidation of 0.1 M ethanol and 0.1 M bioethanol in 0.1 M $HClO_4$ on amorphous (a) $Ni_{59}Nb_{40}Pt_{0.6}Cu_{0.4}$ alloy and (b) $Ni_{59}Nb_{40}Pt_{0.6}Ru_{0.4}$ alloy (temperature 25 °C, sweep rate 50 mV s^{-1}).

3.2.2. Ethanol/bioethanol electrooxidation

Fig. 4 shows the cyclic voltammograms for the different catalysts in the potential range of −0.1 V to 1.5 V (vs. Ag/AgCl) obtained in a 0.1 M $HClO_4$ and 1 M ethanol/bioethanol solution. Before starting electrochemical tests, MCPEs were subjected to repetitive cyclic voltammetry until it got a stable voltammogram. After determining the available catalytic area by cyclic voltammetry in 0.1 M $HClO_4$ media, ethanol was added to obtain the desired concentration, setting the potential to −0.1 V to avoid any parallel process during the addition of alcohol, and the working electrode was submitted to a new experiment by cyclic voltammetry. The bulk is bubbling with nitrogen to prevent the oxidation of the microparticles of electrodes.

Table 2 shows the onset potential (E_{onset}), potential (E_{peak1}, E_{peak2} and E_{peak3}) and current densities (J_{peak1}, J_{peak2} and J_{peak3}) of different peaks. There are small variations in the E_{onset} of different alcohols. For $Ni_{59}Nb_{40}Pt_{0.6}Cu_{0.4}$ alloy, the onset potentials were 0.37 V and 0.39 V, for ethanol and bioethanol respectively. In the case of $Ni_{59}Nb_{40}Pt_{0.6}Ru_{0.4}$ alloy, the onset potentials were 0.45 V and 0.43 V. These values are shifted to more negative potentials compared to the $Ni_{59}Nb_{40}Pt_1$ alloy [8], due to these second metals modifying the electronic properties of Pt, as predicted by the ligand model [17].

For $Ni_{59}Nb_{40}Pt_{0.6}Cu_{0.4}$ alloy higher current densities are obtained than for $Ni_{59}Nb_{40}Pt_{0.6}Ru_{0.4}$ alloy, either by ethanol or by bioethanol oxidation. However, the presence of copper suffers a rapid deactivation in acidic media for the possible formation of oxides of copper, blocking the active sites of platinum, losing efficiency in the electrooxidation. Furthermore, the severe Cu dissolution [18] complicates the electrooxidative process. On the other hand, both alloys provide better current densities for bioethanol electrooxidation, being three times higher than ethanol electrooxidation. By the high performance liquid chromatography (HPLC), it could be mainly detected the presence of acetaldehyde, formic acid and other organic compounds (ppb), which may contribute to improve the catalytic results.

3.2.3. CO tolerance

Other radical species might contribute to the oxidation from parallel reactions, adsorbing on the catalyst surface, resulting in the deactivation of the catalyst and preventing the final oxidation to CO_2. CO is one of the most significant radicals, which is strongly adsorbed on platinum [19], poisoning the available catalytic surface [7–9]. By chrono-amperometric studies of 10 h, the degree of poisoning of the catalyst was found as the electrooxidation of ethanol and bioethanol was in progress. The measurements were performed approximately at first peak potential (0.7 V vs. Ag/AgCl) of cyclic voltammetry.

As it can be observed in Fig. 5, in the first few seconds, the measured current density for bioethanol electrooxidation dropped faster than ethanol oxidation, indicating that the surfaces of catalysts were poisoned with CO rapidly. Furthermore, the presence of acetaldehyde, formic acid and others organic compounds also contributes to increase the poisoning of surface. After 10 h of chrono-amperometric experience, both alloys showed very steady activities. $Ni_{59}Nb_{40}Pt_{0.6}Cu_{0.4}$ alloy showed a higher specific activity of 0.976 mA cm^{-2} and 1.062 mA cm^{-2} for ethanol and bioethanol electrooxidation respectively, whereas $Ni_{59}Nb_{40}Pt_{0.6}Ru_{0.4}$ alloy showed 0.241 mA cm^{-2} and 0.158 mA cm^{-2} respectively.

The obtained chrono-amperograms allowed to set the speed of poisoning of the catalyst [20], expressed as the percentage of poisoned catalyst per second (%s^{-1}) using Eq. (5):

$$\partial(\%s^{-1}) = \left(\frac{100}{J_0}\right) \times \left(\frac{dJ}{dt}\right) \quad (5)$$

Table 2
Onset potential (E_{onset}), potentials (Ep_1, Ep_2 and Ep_3) and current densities (J_1, J_2 and J_3) of different peaks of the different electrodes. 1 M ethanol and 0.1 M bioethanol in 0.1 M $HClO_4$. 0.05 V s^{-1}, 25 °C.

	Ethanol				Bioethanol			
$Ni_{59}Nb_{40}Pt_{0.6}Cu_{0.4}$	E_{onset} 0.45	E_{peak1}, V 0.71	E_{peak2}, V 1.08	$E_{peak\ 3}$, V 0.46	E_{onset} 0.43	E_{peak1}, V 0.74	E_{peak2}, V 1.14	$E_{peak\ 3}$, V 0.46
		J_{peak1}, mA cm^{-2} 0.31	J_{peak2}, mA cm^{-2} 0.39	J_{peak3}, mA cm^{-2} 0.28		J_{peak1}, mA cm^{-2} 0.77	J_{peak2}, mA cm^{-2} 1.01	J_{peak3}, mA cm^{-2} 0.80
$Ni_{59}Nb_{40}Pt_{0.6}Ru_{0.4}$	E_{onset} 0.37	E_{peak1}, V 0.70	E_{peak2}, V 1.04	$E_{peak\ 3}$, V 0.45	E_{onset} 0.39	E_{peak1}, V 0.69	E_{peak2}, V 1.09	E_{peak3}, V 0.41
		J_{peak1}, mA cm^{-2} 1.22	J_{peak2}, mA cm^{-2} 1.40	J_{peak3}, mA cm^{-2} 1.15		J_{peak1}, mA cm^{-2} 3.01	J_{peak2}, mA cm^{-2} 4.30	J_{peak3}, mA cm^{-2} 2.24

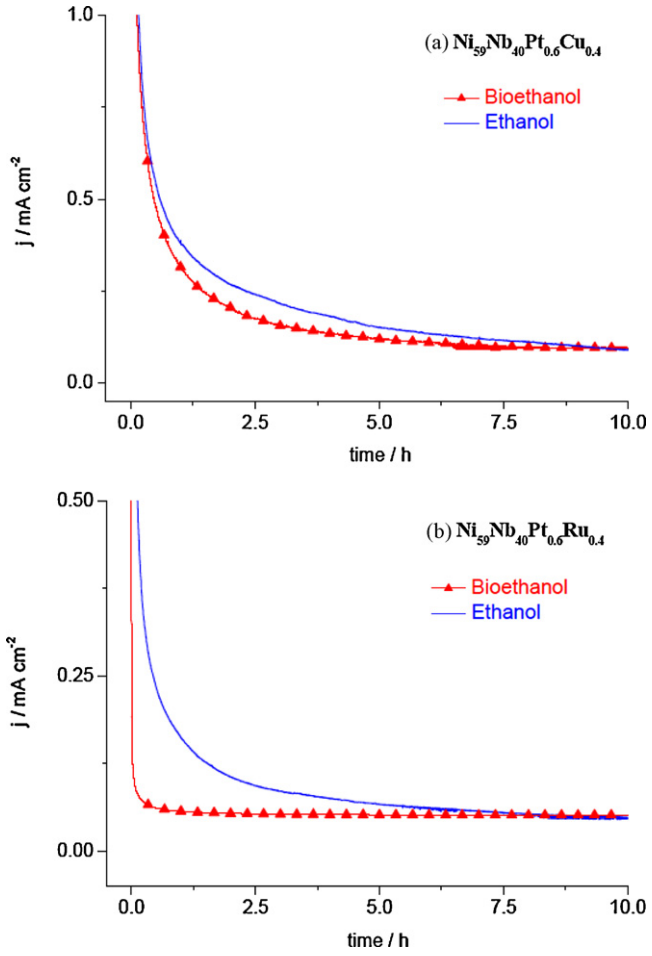

Fig. 5. Current transients for (a) $Ni_{59}Nb_{40}Pt_{0.6}Cu_{0.4}$ alloy and (b) $Ni_{59}Nb_{40}Pt_{0.6}Ru_{0.4}$ alloy. 1 M ethanol and 0.1 M bioethanol in 0.1 M $HClO_4$. 0.7 V polarization potential and 25 °C.

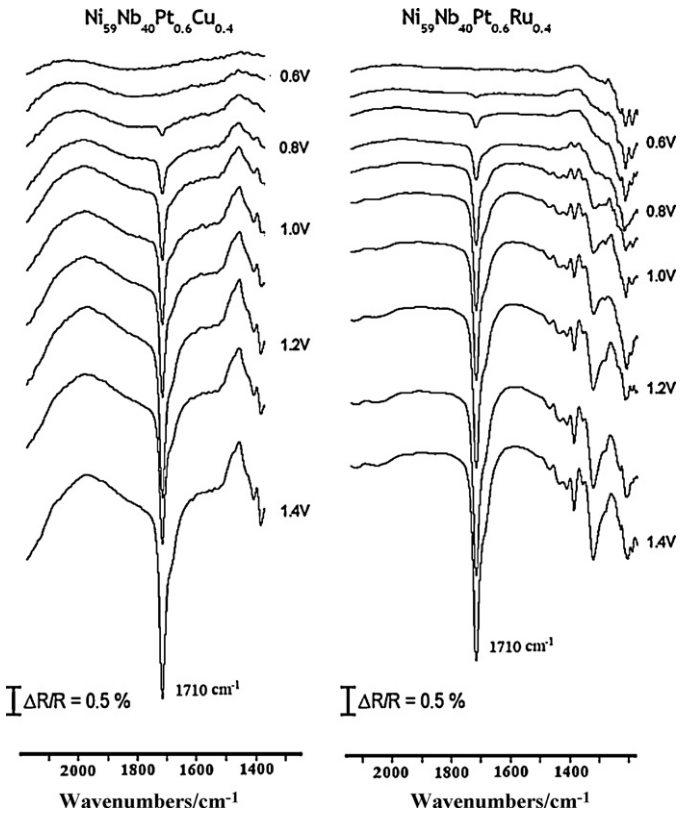

Fig. 6. Sets of in situ FTIR spectra obtained for emergence and evolution of C=O stretching of acetic acid in D_2O for both alloys. Reference potential 0.4 V. Sample potentials indicated for each spectrum in the figure. p-Polarized radiation. 100 interferograms collected at each potential.

where dJ/dt is the slope of the linear portion of the current decay at a given time, and J_0 is the current at the start of polarization back extrapolated from the linear current decay. It is characteristic of these curves that the current density decreases sharply at the beginning of the test, more slowly in the first 10 min and very slowly thereafter. At 10 min time it makes the tangent line to the chrono-amperometric curve and its slope is calculated for all cases. J_0 is given by the cutting of this line with the vertical axis. The resistance to poisoning of active sites for both alloys is clearly observed, being for $Ni_{59}Nb_{40}Pt_{0.6}Cu_{0.4}$ alloy of 0.01%s^{-1} and 0.08%s^{-1} for ethanol and bioethanol electrooxidation respectively, whereas $Ni_{59}Nb_{40}Pt_{0.6}Ru_{0.4}$ alloy were 0.01%s^{-1} and 0.04%s^{-1} respectively.

3.3. Mechanism of electrooxidation. FTIR studies

The complexity of the reaction mechanism of ethanol/bioethanol electrooxidation involves several steps and a number of intermediates and byproducts [21,22]. In obtained voltammograms (Fig. 4) can clearly observe the presence of three oxidation peaks for both alcohols in the investigated range potentials. These peaks are directly related to the different oxidized species during the electrooxidation process. The peak 1 (0.7 V vs. Ag/AgCl) corresponds to the oxidation of ethanol to acetaldehyde. The subsequent oxidation of acetaldehyde to acetic acid is associated to peak 2 (1.1 V vs. Ag/AgCl). Finally, the peak 3 (0.45–0.5 V vs. Ag/AgCl) mainly represents the oxidation of CO to final products CO_2.

Fig. 6 shows one set of in situ FTIR spectra collected for $Ni_{59}Nb_{40}Pt_{0.6}Cu_{0.4}$ and $Ni_{59}Nb_{40}Pt_{0.6}Ru_{0.4}$ alloys in 0.1 M $HClO_4$ and 0.1 M ethanol solutions in D_2O. The processed spectra are displayed after the normalized subtraction of 100 sample interferograms (which were acquired at the sample potentials indicated in Fig. 6) and 100 reference interferograms (collected at 0.4 V vs. RHE for each series). An overview of two spectres of Fig. 6 allows to drawing the several conclusions. It is clearly observe the emergence and evolution of a band (at around 1710 cm^{-1}) corresponding to the C=O stretching of acetic acid. It is detectable at 0.7 V vs. RHE for $Ni_{59}Nb_{40}Pt_{0.6}Cu_{0.4}$ alloy and 0.6 V vs. RHE for $Ni_{59}Nb_{40}Pt_{0.6}Ru_{0.4}$ alloy. The band, which is related to the carbonyl stretching mode, may also be associated with the formation of acetaldehyde, which is further oxidized into acetic acid. From previous works of Iwasita and Pastor [23,24], it is known that ethanol can adsorb on Pt and later acetaldehyde is formed at potentials lower than 0.6 V vs. RHE [25], as follows (6):

$$\begin{aligned} &Pt + CH_3CH_2OH \rightarrow Pt(\bullet CHOHCH_3)_{ads} + H^+ + e^- \\ &Pt(\bullet CHOHCH_3)_{ads} \rightarrow Pt + CH_3CHO + H^+ + e^- \end{aligned} \quad (6)$$

As soon as acetaldehyde is formed, it can adsorb at platinum and forms acetyl radical at $E < 0.4$ V vs. RHE according to reaction (7):

$$Pt + CH_3CHO \rightarrow Pt(\bullet COCH_3)_{ads} + H^+ + e^- \quad (7)$$

This acetyl radical could follow two paths. One alternative would be the formation of acetic acid. At potentials higher than 0.6 V vs. RHE, the water molecule is dissociated to form oxygenated species at the platinum surface, which are able to oxidize acetyl radical to acetic acid, as follows (8):

$$Pt(\bullet COCH_3)_{ads} + Pt(OH)_{ads} \rightarrow 2Pt + CH_3COOH \quad (8)$$

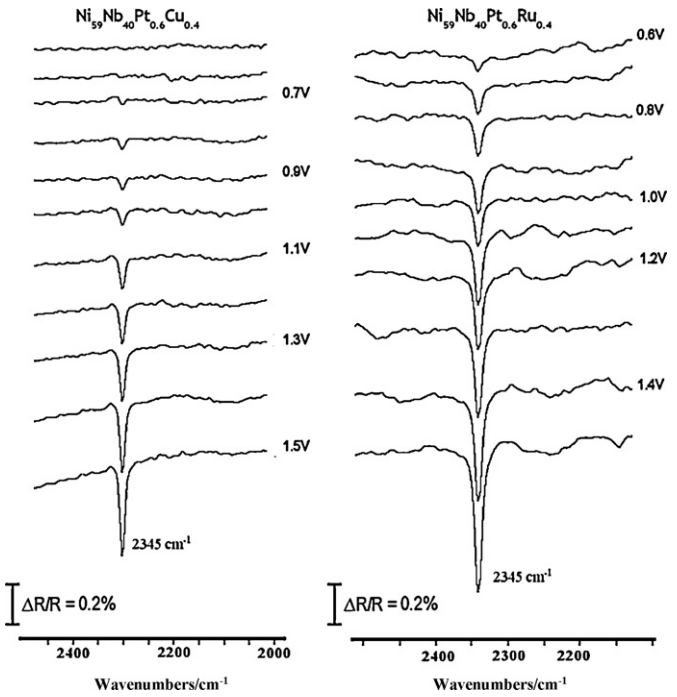

Fig. 7. Sets of in situ FTIR spectra obtained for emergence and evolution of CO_2 for both alloys. Reference potential 0.4 V. Sample potentials indicated for each spectrum in the figure. p-Polarized radiation. 100 interferograms collected at each potential.

The second path would be the homolytic cleavage of C–C bond being formed CO species adsorbed on platinum [23] at $E > 0.3$ V vs. RHE. Together with oxygenated species, CO_2 is formed, as follows (9):

$$\begin{aligned} &Pt + Pt(^{\bullet}COCH_3)_{ads} \rightarrow Pt(CO)_{ads} + Pt(CH_3)_{ads} \\ &Pt(CO)_{ads} + Pt(OH)_{ads} \rightarrow 2Pt + CO_2 + H^+ + e^- \end{aligned} \quad (9)$$

Fig. 7 shows the emergence and evolution of CO_2 for $Ni_{59}Nb_{40}Pt_{0.6}Cu_{0.4}$ and $Ni_{59}Nb_{40}Pt_{0.6}Ru_{0.4}$ alloys in 0.1 M $HClO_4$ and 0.1 M ethanol solutions. An adsorption band at around 2345 cm^{-1} corresponding to CO_2 is clearly observed. It is detectable at 0.7 V vs. RHE for $Ni_{59}Nb_{40}Pt_{0.6}Cu_{0.4}$ alloy and 0.6 V vs. RHE for $Ni_{59}Nb_{40}Pt_{0.6}Ru_{0.4}$ alloy.

The integrated intensity from acetic acid spectra with the applied potentials is shown in Fig. 8. It is clearly derived

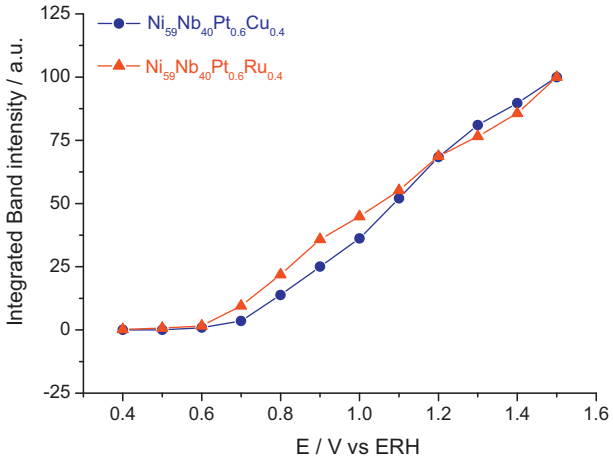

Fig. 8. Potential dependence of the integrated band intensity for acetic acid (signal about 1710 cm^{-1}) obtained from 0.1 M Ethanol electrooxidation on different amorphous metallic alloys.

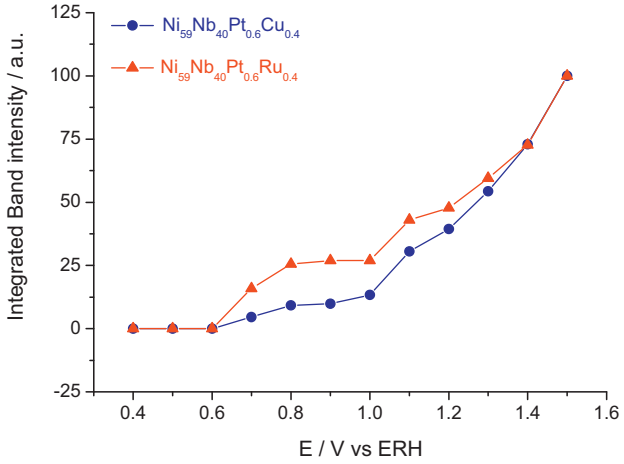

Fig. 9. Potential dependence of the integrated band intensity for CO_2 (signal about 2345 cm^{-1}) obtained from 0.1 M Ethanol electrooxidation on different amorphous metallic alloys.

that $Ni_{59}Nb_{40}Pt_{0.6}Ru_{0.4}$ alloy has E_{onset} more negative than $Ni_{59}Nb_{40}Pt_{0.6}Cu_{0.4}$ alloy for ethanol electrooxidation. However the rate of production of acetic acid is slightly higher for alloys with Cu. Fig. 9 shows the integrated intensity of CO_2 at different potentials. The alloy with Ru catalyzes the oxidation of ethanol to CO_2 in a higher proportion than the alloy with Cu at low-middle potentials. Therefore, the addition of Ru catalyzes the reaction to CO_2 at higher rates than the alloy with Cu, being the ratio of acetic acid/CO_2 smaller for $Ni_{59}Nb_{40}Pt_{0.6}Ru_{0.4}$ alloy, so the presence of Cu mainly leads to the formation of acetic acid. The question is whether the acetic acid can be oxidized to CO_2. Preliminary studies show oxidation spectra of acetic acid to CO_2, for both alloys. These facts must be studied more in depth by differential electrochemical mass spectroscopy (DEMS) and FTIR to verify that the amorphous metallic alloys are able to cleavage of C–C bond of acetic acid.

4. Conclusions

This work presents some evidence of in situ FTIR and electrochemical measurements to support a mechanism of ethanol/bioethanol electooxidation on amorphous alloys of composition $Ni_{59}Nb_{40}Pt_{0.6}Cu_{0.4}$ and $Ni_{59}Nb_{40}Pt_{0.6}Ru_{0.4}$. These alloys were contained as MCPEs to study their catalytic behavior in the reaction of ethanol/bioethanol electrooxidation. The addition of Cu and Ru, as co-catalysts, modifies the electronic properties of platinum, making an improvement on energetic efficiency and increasing tolerance on adsorbed species, such as CO. It is noted that electrooxidation of bioethanol provides better current densities than ethanol due to the presence of impurities (acetaldehyde, acid formic...) which may contribute to that improvement. The catalytic activity is higher for the $Ni_{59}Nb_{40}Pt_{0.6}Cu_{0.4}$ alloy however the presence of the copper suffers a rapid deactivation in acidic medium for the possible dissolution and formation of oxides of copper, blocking the active sites of platinum.

Electrooxidation of ethanol/bioethanol is a very complex process because several reaction products and intermediates can be formed. The final products are CO_2 (with transfer of $12e^-$) and acetic acid (with transfer of $4e^-$). By FTIR studies, the onset potential of alloy with Ru (0.6 V vs. RHE) is lower than the alloy with Cu (0.7 V vs. RHE). The presence of Ru catalyzes the reaction to CO_2 at higher rates than the alloy with Cu, being the ratio of acetic acid/CO_2 smaller for $Ni_{59}Nb_{40}Pt_{0.6}Ru_{0.4}$ than $Ni_{59}Nb_{40}Pt_{0.6}Cu_{0.4}$ alloy.

Acknowledgements

The authors acknowledge the financial support to MEC (CTQ2006-13163/BQU and MAT2007-60621), the DFG (94/2008) and Basque Government (IT515-10). We also want to acknowledge here the contribution of Prof. Dr. Juan José del Val Altuna who worked in the study of XRD.

References

[1] C. Lamy, E.M. Belgsir, J.-M. Léger, J. Appl. Electrochem. 31 (2001) 799–809.
[2] S. Rosseau, C. Coutanceau, C. Lamy, J.-M. Léger, J. Power Sources 158 (2006) 18–24.
[3] F. Vigier, S. Rousseau, C. Coutanceau, J.-M. Léger, C. Lamy, Top. Catal. 40 (1–4) (2006) 111–121.
[4] C. Coutanceau, S. Brimaud, C. Lamy, J.-M. Léger, L. Dabau, S. Rousseau, F. Vigier, Electrochim. Acta 53 (2008) 6865–6880.
[5] M. Sistiaga, A.R. Pierna, J. Non-Crystal. Solids 329 (2003) 184–187.
[6] A.R. Pierna, M. Sistiaga, C. Navascués, A. Lorenzo, J. Non-Crystal. Solids 287 (2001) 432–436.
[7] J. Barranco, A.R. Pierna, J. Non-Crystal. Solids 353 (2007) 851–854.
[8] J. Barranco, A.R. Pierna, J. New Mater. Electrochem. Syst. 12 (2&3) (2009) 69–76.
[9] J. Barranco, A.R. Pierna, J. Power Sources 169 (2007) 71–76.
[10] S. Luis Gustavo, Pereira, A. Valdecir, Paganin, A. Edson, Ticianelli, Electrochim. Acta 54 (2009) 1992–1998.
[11] P. Pietro, Lopes, A. Edson, Ticianelli, J. Electroanal. Chem. 644 (2) (2010) 110–116.
[12] C.C. Koch, O.B. Cavin, C.G. Mckamey, J.O. Scarbrough, Appl. Phys. Lett. 43 (1983) 11.
[13] P.Y. Lee, C.C. Koch, J. Non-Crystal. Solids 94 (1987) 88–100.
[14] J.Y. Huot, L. Brossard, Int. J. Hydrogen Energy 12 (1987) 599.
[15] M. Metikos-Hukovic, A. Jukic, Electrochem. Acta 45 (2000) 4159.
[16] T. Vidaković, M. Christov, K. Sundmacher, Electrochim. Acta 52 (2007) 5606–5613.
[17] T. Iwasita, Electrochim. Acta 47 (2002) 3663.
[18] T. Page, R. Johnson, J. Hormes, S. Noding, B. Rambabu, J. Electroanal. Chem. 485 (2000) 34.
[19] Junhua Jiang, Anthony Kucernak, J. Electroanal. Chem. 543 (2003) 187–199.
[20] G. García, J.A. Silva-Chong, O. Guillén-Villafuerte, J.L. Rodríguez, E.R. González, E. Pastor, Catal. Today 116 (2006) 415–421.
[21] F.C. Simões, D.M. dos Anjos, F. Vigier, J.-M. Léger, F. Hahn, C. Coutanceau, E.R. Gonzalez, G. Tremiliosi-Filho, A.R. Andrade, P. Olivi, K.B. Kokoh, J. Power Sources 167 (2007) 1–10.
[22] F. Vigier, C. Coutanceau, F. Hahn, E.M. Belgsir, C. Lamy, J. Electroanal. Chem. 563 (2004) 81–89.
[23] T. Iwasita, E. Pastor, Electrochim. Acta 39 (1994) 531.
[24] T. Iwasita, E. Pastor, Electrochim. Acta 39 (1994) 547.
[25] H. Hitmi, E.-M. Belgsir, J.-M. Léger, C. Lamy, R.O. Lezna, Electrochim. Acta 39 (1994) 407.